coatings

MDPI

Article

A Superhydrophobic Anti-Icing Surface with a Honeycomb Nanopore Structure

Bo Li [1], Huiying Xiang [2], Xu Dai [3], Tao Zhu [2], Xujiang Hua [2] and Yuan Yuan [2,*]

[1] Institute of Electric Power Science of Guizhou Power Grid Co., Ltd., Guiyang 550002, China; gzgylb2207@163.com
[2] College of Materials Science and Engineering, Chongqing University, Chongqing 400030, China; 20200901052@cqu.edu.cn (H.X.); davezhu@cqu.edu.cn (T.Z.); 20230901040@stu.cqu.edu.cn (X.H.)
[3] State Key Laboratory of Power Transmission Equipment & System Security and New Technology, Chongqing University, Chongqing 400044, China; xudai@cqu.edu.cn
* Correspondence: yuany@cqu.edu.cn

Abstract: Recently, the icing disaster of transmission lines has been a serious threat to the safe operation of the power system. A superhydrophobic (SHP) anti-icing surface with a honeycomb nanopore structure was constructed using anodic oxidation technology combined with a vacuum infusion process. When the current density was 87.5 mA/cm^2, the honeycomb porous surface had the best superhydrophobic performance (excellent water mobility), lowest ice-adhesion strength (0.7 kPa) and best anti-frosting performance. Compared with other types of alumina surfaces, the ice-adhesion strength of the SHP surface (87.5 mA/cm^2) was only 0.2% of that of the bare surface. The frosting time of the SHP surface (87.5 mA/cm^2) was 150 min, which was much slower. The former is attributed to the air cushion within the porous structure and the stress concentration, and the latter is attributed to the self-transition of the droplets and low solid–liquid heat transfer area. After 100 icing or frosting cycles, the SHP surface (87.5 mA/cm^2) maintained a low ice-adhesion strength and superhydrophobic performance. This is because the anodic oxidation process forms a hard porous film, and the nano porous structure with a high aspect ratio can store modifiers to realize self-healing. The results indicate that the SHP surface with a honeycomb nanopore structure presents excellent anti-icing performance and durability.

Keywords: superhydrophobic; anti icing; honeycomb nanopore structure

Citation: Li, B.; Xiang, H.; Dai, X.; Zhu, T.; Hua, X.; Yuan, Y. A Superhydrophobic Anti-Icing Surface with a Honeycomb Nanopore Structure. *Coatings* **2023**, *13*, 1971. https://doi.org/10.3390/coatings13111971

Academic Editor: Alexander Tolstoguzov

Received: 16 October 2023
Revised: 15 November 2023
Accepted: 16 November 2023
Published: 20 November 2023

1. Introduction

To promote the transformation of clean energy and achieve carbon peak and carbon neutrality, an important development strategy of building a 'new power system' has been proposed in China, aiming to realize multi-energy complementarity under the basic premise of energy and power security. In the process of building a 'new power system', large-capacity, long-distance ultra-high voltage (UHV) transmission lines inevitably pass through harsh areas such as severe icing. The icing disaster of transmission lines is one of the most serious threats to the safe operation of the power system. The harsh climate and traffic conditions during an ice disaster make the repair process extremely difficult, resulting in a long outage time and greater economic losses and social impact [1–4]. According to the statistics of the power sector, China's transmission line failures caused by icing have reached nearly a thousand since 1950. Therefore, it is extremely urgent and necessary to develop effective and reliable de-icing and anti-icing technologies for transmission lines.

At present, the actual icing prevention measures in actual application are mainly divided into two categories: de-icing and anti-icing. De-icing methods mainly include the high-current de-icing method and mechanical de-icing method [5–8], that is, to remove the existing icing. These methods cannot inhibit the formation of icing in the early stages of icing, and they often cause major safety accidents on transmission lines after large-scale icing.

The anti-icing methods, such as coating or surface treatment technologies, are based on the properties of the material itself for inhibiting or slowing down the continuous formation of icing, which can fundamentally reduce the incidence of icing accidents. These methods are increasingly being recognized [9,10]. Among them, the superhydrophobic (SHP) coating or surface based on bionic technology can use its excellent hydrophobic properties to reduce water droplet adhesion, delay icing time and reduce ice adhesion strength [11,12], which is expected to achieve the intrinsic permanent anti-icing performance of transmission lines [13]. However, the current SHP coating or surface still faces technical bottlenecks that are difficult to overcome. First, in a low-temperature and high-humidity environment with severe icing, condensation and frosting occur on the microstructure, resulting in the loss of anti-icing effectiveness [14]. Second, the coating or surface generally has the problem of poor wear resistance and poor adhesion between the film and the substrate, resulting in poor anti-icing durability [15,16]. Therefore, the development of new SHP surfaces for the above two points is the key to breaking through the existing technical bottlenecks.

In this study, a durable anti-icing alumina surface with a honeycomb nanopore structure was constructed using anodic oxidation technology combined with a vacuum infusion process. By adjusting the current density of the anodic oxidation, porous structures with different microstructures were constructed, and the optimal process parameters were screened using wettability and anti-icing performance. The anti-icing durability of the SHP surface with a honeycomb nanopore structure under multi-cycle damage was studied.

2. Materials and Methods

2.1. Materials

A total of 1060 aluminum plates were used as substrate materials, and the size of each plate was 20 mm × 20 mm × 1 mm. The aluminum plates were purchased from Dongguan Chaomei Aluminum Products Co., Ltd., Shijiazhuang, China. Ethanol, sodium hydroxide, phosphoric acid and oxalic acid were purchased from Chongqing Chuandong Chemical Co., Ltd., Chongqing, China. 1H,1H,2H,2H-Perfluorodecyltrimethoxysilane (FAS) was purchased from Shanghai Aladdin Reagent Co., Ltd., Shanghai, China.

2.2. Fabrication

Two layers of porous structures were constructed on the surface of 1060 pure aluminum plates through two-step anodization. The preparation process included pretreatment, anodic oxidation and modifier injection and curing. (1) Pretreatment. The aluminum sheet was immersed in sodium hydroxide solution (1 mol/L) for 5 min to remove the grease and oxide film. Then, the sheet was ultrasonically cleaned with pure water. (2) Anodic oxidation. The treated aluminum sheet was used as the anode, and the stainless-steel sheet was used as the cathode. The first step of oxidation was carried out in a phosphoric acid solution (0.3 mol/L), and the second step of oxidation was carried out in an oxalic acid solution (0.15 mol/L). The current density and oxidation time were regulated using a DC power supply. Specifically, the current density range of the first step was 62.5–100.0 mA/cm^2, and the oxidation time was 10 min. The current density and time of the second step were 43.7 mA/cm^2 and 15 min, respectively. The temperature in the electrolyte was controlled using an industrial chiller. The anodic aluminum oxide (AAO) was immersed in the modifier (FAS) and kept in vacuum for 3 h. The excess FAS on the sample was removed with a fan, and the air cushion on the surface of the porous structure was retained. Finally, the FAS was solidified in an oven at 90 °C for 30 min to obtain a durable anti-icing alumina surface with a two-layer porous structure. Additionally, the untreated aluminum (bare) and the bare-FAS surfaces were used for comparison. The bare-FAS was prepared by grafting low-surface-energy molecules on the bare surface. Specifically, the bare sample was immersed in the FAS- ethanol solution (2 wt%) for 30 min. Then, the sample was taken out and placed in a drying oven at 90 °C for 30 min to obtain a bare-FAS surface.

2.3. Characterization

The surface morphology of the samples was characterized through focused ion beam field-emission double-beam scanning electron microscopy (Zeiss Auriga, Oberkochen, Germany, SEM). Before the test, the surface was sprayed with gold (10 nm) to enhance the conductivity of the sample. The surface roughness was measured via laser confocal microscopy (Olympus, Tokyo, Japan, LEXT OLS4000). The pore size, porosity and oxide film thickness of the surface were obtained by analyzing the morphology images using ImageJ software. The contact angle (CA) and contact angle hysteresis (CAH) of the surface were measured using a contact angle measuring instrument (SINDIN, Dongguan, China, SDC-100). The droplet size for CA measurement was 5 μL. The CAH is the difference between the advancing angle and the receding angle (5 μL). The advancing and receding angles were measured using the change in droplet volume. The measurements of CA and CAH were performed on three parallel samples, and the mean values were calculated.

The frosting process was carried out on a high-precision semiconductor constant-temperature experimental platform (LTD 1–350). The samples were subjected to condensation and frosting at −3 °C, and the ambient humidity was 79% RH. The surface frosting morphology was recorded with a camera.

A homemade platform composed of a high-precision semiconductor constant-temperature experimental platform and a digital push–pull meter was built to measure the ice-adhesion strength (Scheme 1). In detail, the semiconductor-platform temperature was set to −3 °C. The ambient temperature and humidity were 25 °C and 50% RH, respectively. A polytetrafluoroethylene cylinder mold with a diameter of 0.7 cm was placed on the surface of the sample, and 1 mL of deionized water was injected into the mold. Then, the sample was cooled to −10 °C for 15 min by the semiconductor platform. A hand-shaking test bracket was used to push the cylindrical mold at a constant rate to separate it from the sample surface. The maximum value shown by the push–pull meter was the ice-adhesion force. The ice-adhesion force divided by contact area was the ice-adhesion strength. The measurement of the ice-adhesion strength was performed on three parallel samples, and the mean values were calculated.

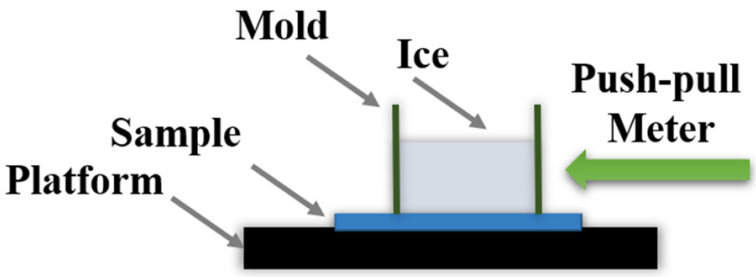

Scheme 1. Test device for ice-adhesion strength.

Icing/melting and frosting/melting cycles were conducted on the semiconductor platform to evaluate the anti-icing durability of the samples. For the icing/melting cycles, the freezing process was the same as the test procedure of the ice-adhesion strength, that is, water was put into the cylindrical mold. When the water was frozen, the temperature of the semiconductor increased to 20 °C to melt the ice. The icing/de-icing process was repeated to evaluate the anti-icing durability. For the frosting/melting cycles, the sample was placed on the platform, and the ambient humidity was maintained at 79% through the humidifier. When the water vapor condensed and frosted on the surface, the temperature of the semiconductor increased to 20 °C to melt the frost. The icing/de-icing process was repeated.

3. Results

3.1. Morphology and Wettability

Figure 1 shows the surface and cross-sectional morphologies of the sample at different current densities in the first step of anodic oxidation. The pore size, pore wall thickness and porosity of the porous surface were calculated using ImageJ software. The gap ratio is the ratio of pore size to pore wall thickness. With the increase in current density, the pore size increased significantly from 210 to 300 nm and then tended to be stable. In addition, as the current density increased from 62.5 to 100.0 mA/cm^2, the porosity increased from 65% to 75%, and the gap ratio increased from 4.67 to 12.50. When the current density reached 87.5 mA/cm^2, protrusions and depressions began to appear on the flat surface. The shape of the pore structure gradually changed from an oval to a hexagonal honeycomb. Herein, the double-layer porous structure was prepared using two-step oxidation. The nano-porous structure was used to store the low-surface-energy modifier (FAS) to repair the loss of the modifier on the SHP surface under external damage (such as de-icing cycles). The double-layer structure with a high aspect ratio (the ratio of thickness to pore size) can increase the storage capacity of FAS as much as possible, thereby enhancing the anti-icing durability of the SHP surface. It can be seen from the cross-sectional morphology that the current density of the first step of anodic oxidation mainly affected the film thickness of the upper-layer pore, and the thickness of the lower-layer pore was maintained at 13–15 μm. With the increase in current density, the thickness of the upper pore increased from 6.83 to 27.07 μm, and the aspect ratio increased from 37.94 to 90.23. In summary, when the current density of the first step of anodic oxidation was higher than 87.5 mA/cm^2, the honeycomb nanopore structure with a high aspect ratio was prepared.

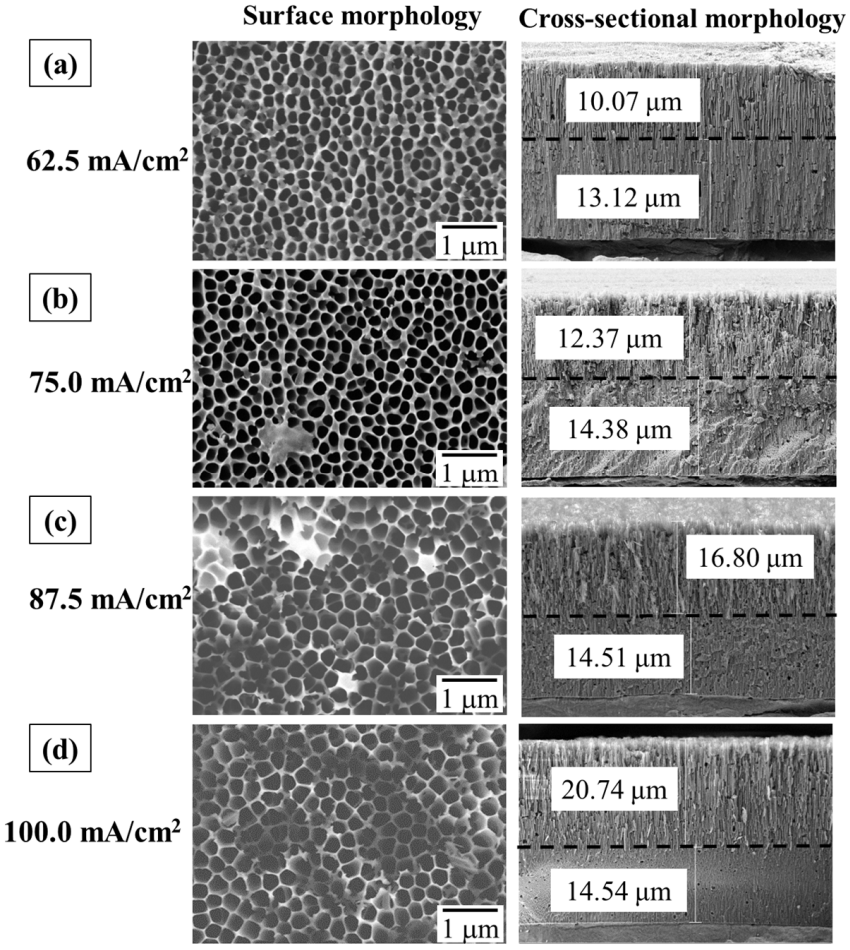

Figure 1. Surface morphology and cross-sectional morphology of the SHP surfaces at different current densities, (**a**) 62.5 mA/cm^2, (**b**) 75.0 mA/cm^2, (**c**) 87.5 mA/cm^2, (**d**) 100.0 mA/cm^2.

Roughness is one of the important factors affecting the surface properties of samples. The three-dimensional morphology and roughness of the sample surface at different current densities in the first step of anodic oxidation were observed using laser confocal microscopy, and the results are shown in Figure 2. When the current density was not more than 75.0 mA/cm^2, the sample surface was relatively smooth, and the maximum roughness was 0.576 µm. As the current density increased, the surface roughness of the sample gradually increased. When the current density was 100.0 mA/cm^2, the roughness increased rapidly to 0.946 µm. Therefore, the increase in current density not only increases the pore size and porosity, but also increases the surface roughness, which is conducive to the realization of excellent superhydrophobic properties on the surface.

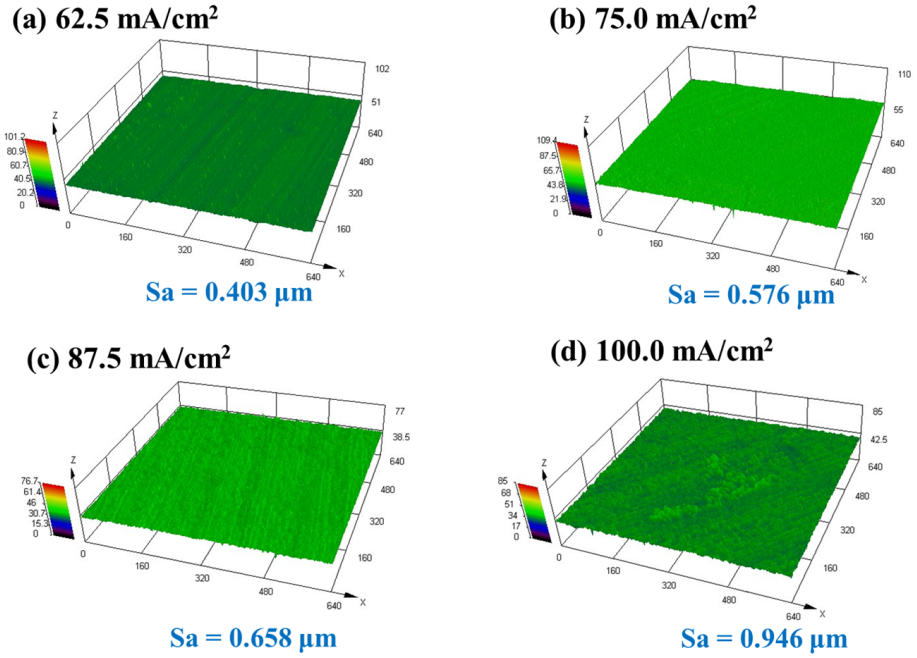

Figure 2. Three-dimensional morphology and roughness of the SHP surfaces at different current densities, (**a**) 62.5 mA/cm^2, (**b**) 75.0 mA/cm^2, (**c**) 87.5 mA/cm^2, (**d**) 100.0 mA/cm^2.

The CA and CAH of water droplets are some of the important parameters to characterize the wettability of the sample surface. As shown in Figure 3a,b, the current density of the first step of anodization significantly affected the wettability of the SHP surface. When the anodic oxidation current increased from 62.5 to 87.5 mA/cm^2, the CA increased from 159° to 173°, and CAH decreased from 3.4° to 0.1°. Larger CAs can reduce the solid–liquid contact area and heat exchange, which is beneficial to prolong the time required for icing. Meanwhile, the reduction of the solid–liquid contact point can concentrate the icing stress and reduce the ice-adhesion strength. In addition, the smaller the CAH, the more easily the water droplets leave the surface, which is conducive to reducing the surface icing [15,17]. As the current density increased to 100.0 mA/cm^2, the CA decreased to 164°, and the CAH increased to 2.8°. This is due to the excessive dissolution of the surface pore structure caused by excessive current density. The resulting micron-scale rough structure reduces the hydrophobic performance, which leads to the decrease in CA and the increase in CAH. Therefore, when the current density was 87.5 mA/cm^2, the porous surface had the best superhydrophobic performance.

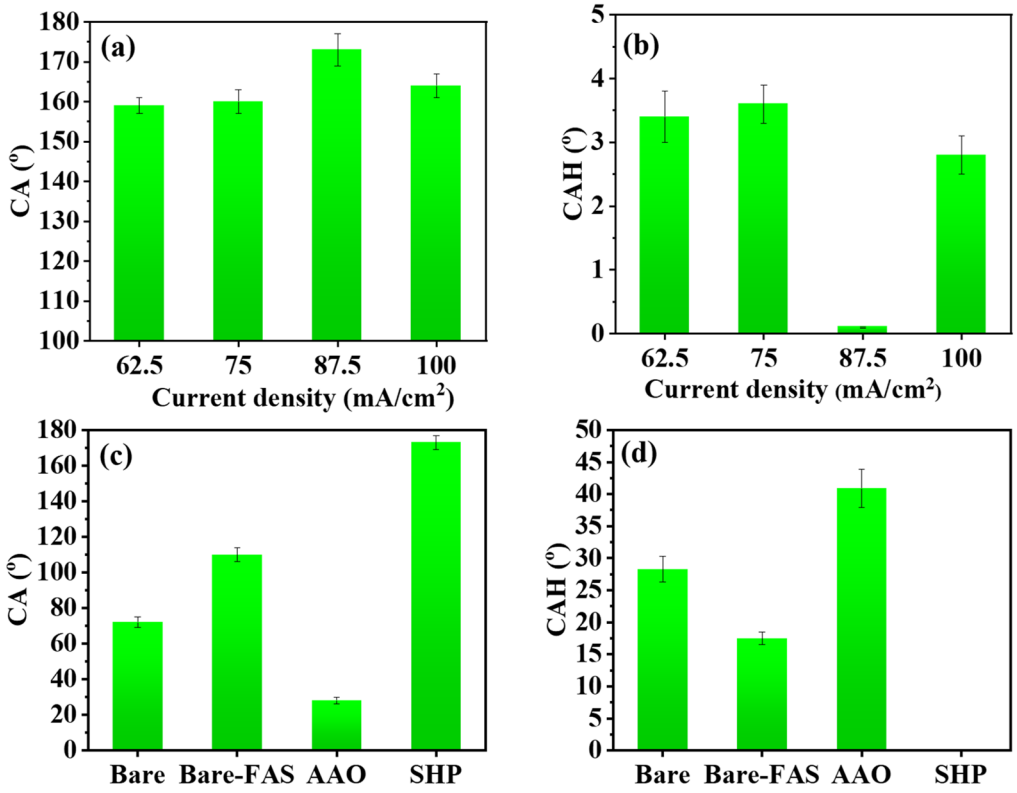

Figure 3. (**a**) CA and (**b**) CAH of the SHP surfaces at different current densities. (**c**) CA and (**d**) CAH of different types of alumina surfaces (87.5 mA/cm^2).

The wettability of different types of alumina surfaces is shown in Figure 3c,d. The CA of the bare was 72°, and the CAH was 28.3°. When the bare plate was modified with FAS, the CA increased to 102°, and the CAH decreased to 17.5°. For AAO without modification, the CA decreased significantly to 28°, and the CAH increased to 40.9°. This is because water droplets are easily embedded in micro-nano pores to form a Wenzel state. For the AAO with modification (SHP), the CA increased to 173°, and the CAH decreased to 0.122°. The large-pore structure of the surface captures air to form a cushion between the water droplet and the alumina surface, so that the droplet forms a Cassie state on the SHP surface. Therefore, compared with different types of alumina surfaces, the SHP surface has excellent water droplet mobility.

3.2. Anti-Icing Performance

The low ice adhesion strength value makes the ice on the sample surface fall off under its own gravity or external force. Ice adhesion of less than 10 kPa is defined as ultra-low ice-adhesion strength [18]. The ice-adhesion strength of the samples at different current densities in the first step of anodic oxidation was measured, and the results are shown in Figure 4a. As the current density increased, the ice-adhesion strength decreased from 13.2 to 0.7 kPa. This is because the increase in porosity and gap ratio of the porous structure improves superhydrophobic performance. When the current density continued to increase to 100.0 mA/cm^2, the ice-adhesion strength increased rapidly to 12.3 kPa. This is because when the current density is too high, a micron-scale rough structure is formed on the surface, and the condensed water droplets are embedded in the structure to form a Wenzel state, resulting in an interlocking effect. This leads to a rapid increase in ice adhesion strength. In summary, the SHP surface obtained an extremely low ice-adhesion strength at a current density of 87.5 mA/cm^2.

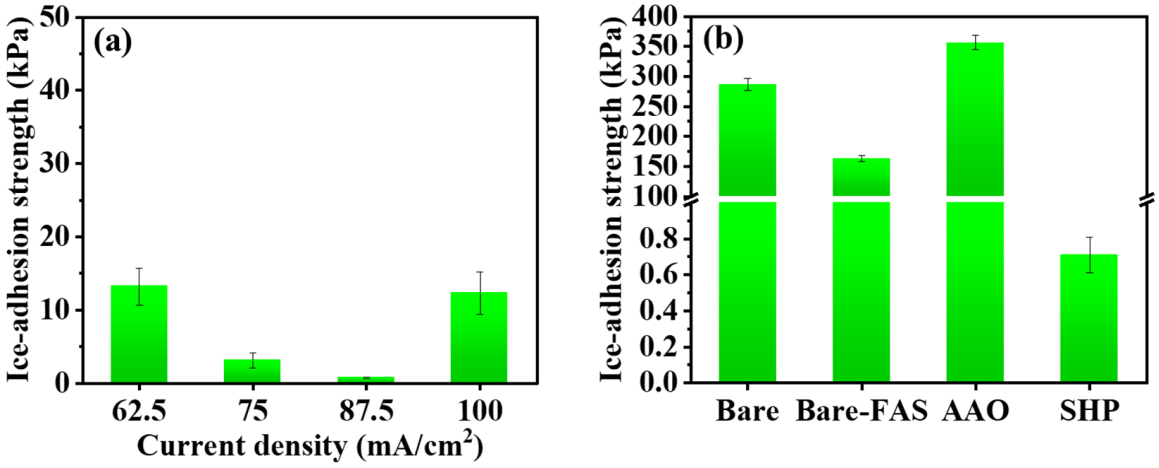

Figure 4. Ice-adhesion strength of (**a**) the SHP surfaces at different current densities and (**b**) different types of alumina surfaces (87.5 mA/cm^2).

The ice-adhesion strength of different types of alumina surfaces is shown in Figure 4b. The ice-adhesion strength of the bare aluminum plate was 287.0 kPa. After modification with a low-surface-energy material (FAS), the ice-adhesion strength of the bare FAS decreased to 163.0 kPa. For the unmodified AAO surface, water quickly entered the pores after contacting the surface, and the Wenzel state was formed after freezing, which greatly increased the interlocking effect between the rough structure and the water. This resulted in the rapid increase in the ice-adhesion strength to 357.1 kPa. The ice-adhesion strength of the modified AAO surface, namely, SHP surface (87.5 mA/cm^2), was significantly reduced to 0.71 kPa, which is only 0.2% of that of the bare surface. The low ice-adhesion strength of the prepared SHP surface is attributed to two factors. First, the nano porous structure captures air to form an air cushion between water and the surface, which significantly reduces the contact area between ice and the solids. On the other hand, due to the influence of pore structure, water can cause stress concentration and micro cracks after freezing, which reduces the ice adhesion between ice and the alumina surface.

In the environment of a low temperature and high humidity, anti-icing SHP surfaces are prone to condensation and frosting, resulting in hydrophobic failure. Thus, the anti-frosting performance of the prepared SHP surface is particularly important. Frosting experiments were carried out on a semiconductor platform (temperature −3 °C, humidity 79% RH). The macroscopic morphology of the sample surface under different frosting times and the complete frosting time were recorded. The results are shown in Figure 5. When the frosting time was 30 min, only dispersed spherical condensate droplets appeared on the SHP surface with a current density of 87.5 mA/cm^2 (Figure 5c), and no obvious frost crystals were formed. The frosting phenomenon appeared on the other sample surfaces, and the frost crystals grew from the edge of the sample to the middle (Figure 5a,b,d). When the frosting time was 120 min, the frost crystals appeared from the edge of the SHP surface (87.5 mA/cm^2). Notably, the middle part was not covered by frost, and spherical liquid water droplets remained. By contrast, the surface of the remaining samples was completely covered by frost crystals. As shown in Figure 5e, with the increase in current density, the frosting time of the sample increased first and then decreased. When the current density was 87.5 mA/cm^2, the frosting time of the SHP surface reached the maximum of 150 min. The frosting time is related to the hydrophobicity of the surface. The better the hydrophobicity, the easier the condensation water droplets form the Cassie state on the surface. The Cassie-state droplets can reduce the contact area between the liquid and the surface, thereby reducing the heat transfer. The SHP surface with 87.5 mA/cm^2 had the best superhydrophobic properties and, thus, had the longest frosting time. In summary, the SHP surface showed excellent anti-frosting performance when the current density was 87.5 A/cm^2.

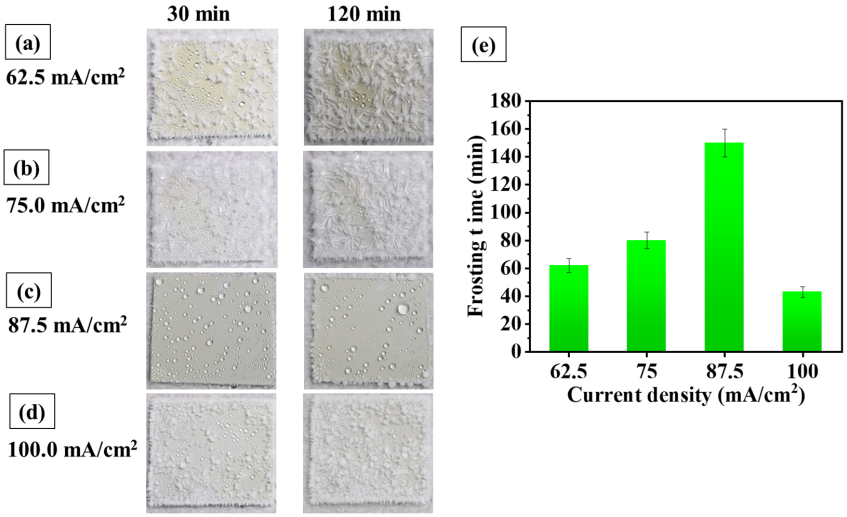

Figure 5. Frosting morphology of the SHP surfaces at different current densities, (**a**) 62.5 mA/cm^2, (**b**) 75.0 mA/cm^2, (**c**) 87.5 mA/cm^2, (**d**) 100.0 mA/cm^2. (**e**) Frosting time of the SHP surfaces at different current densities.

The frosting morphology and frosting time of different types of alumina surfaces at a temperature of −3 °C and a humidity of 79% RH are shown in Figure 6. The frosting rate of the bare and the unmodified AAO surfaces was fast, and these surfaces were each completely covered by frost crystals at 10 min. After the bare surface was modified with a low surface energy, the frosting time was delayed to 30 min. The frosting rate of the SHP surface was much slower than that of other samples, and the surface was completely covered by frost crystals after 150 min of frosting. The condensation and frosting process is related to the micro-nano rough structure and surface energy state. The droplets are in the Cassie condensation state on the SHP surface, which is prone to self-transition. This results in a long distance between the water droplets, and the frost does not easily expand rapidly. Furthermore, the SHP surface has a low solid–liquid heat transfer area, which greatly delays the condensation and freezing of water droplets.

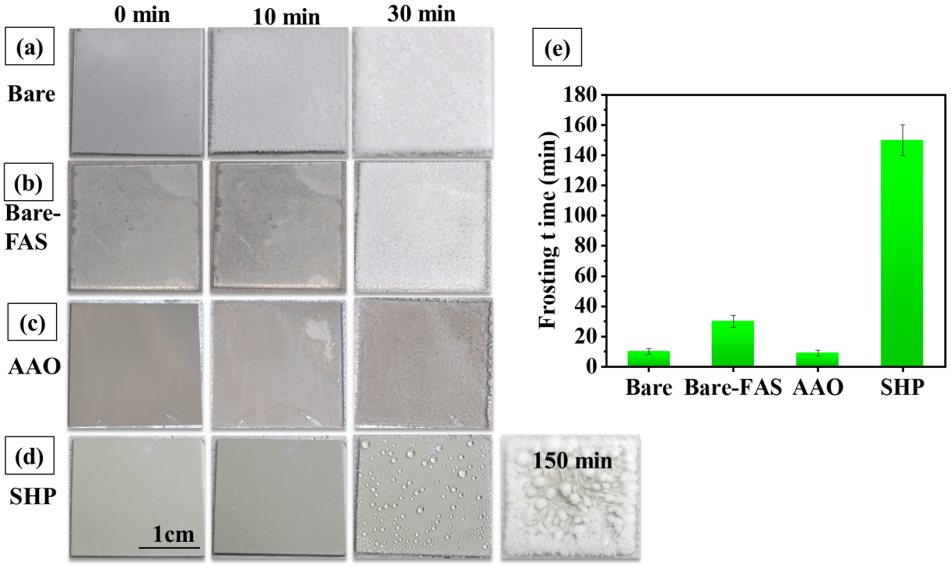

Figure 6. Frosting morphology of different types of alumina surfaces (87.5 mA/cm^2), (**a**) bare, (**b**) bare-FAS, (**c**) AAO and (**d**) SHP. (**e**) Frosting time of different types of alumina surfaces.

From the above results, the optimal current density of the first-step anodic oxidation is 87.5 mA/cm^2, and the SHP surface exhibits the best anti-icing performance. Subsequently, the anti-icing durability test was carried out with the optimal SHP surface (87.5 mA/cm^2).

3.3. Anti-Icing Durability

Transmission lines are inevitably subjected to the physical-damage process of icing and frosting under normal operating conditions. To explore the performance changes of the SHP surface after repeated icing and frosting, 100 icing/melting and frosting/melting cycles were carried out, respectively. The ice-adhesion strength of the SHP surface as well as CA and CAH were tested every 10 cycles.

The change in ice-adhesion strength of the SHP surface with the icing/melting cycle is shown in Figure 7a. As the number of icing/melting cycles increased, the ice-adhesion strength of the sample gradually increased. The initial ice-adhesion strength of the SHP surface was 0.71 kP, which increased to 11.9 kPa after the 100th cycle, which was still far below the critical value of 20 kPa for ice self-removal on the anti-icing surface [19]. The results show that the prepared SHP surface has excellent durability during multi-cycle icing and melting.

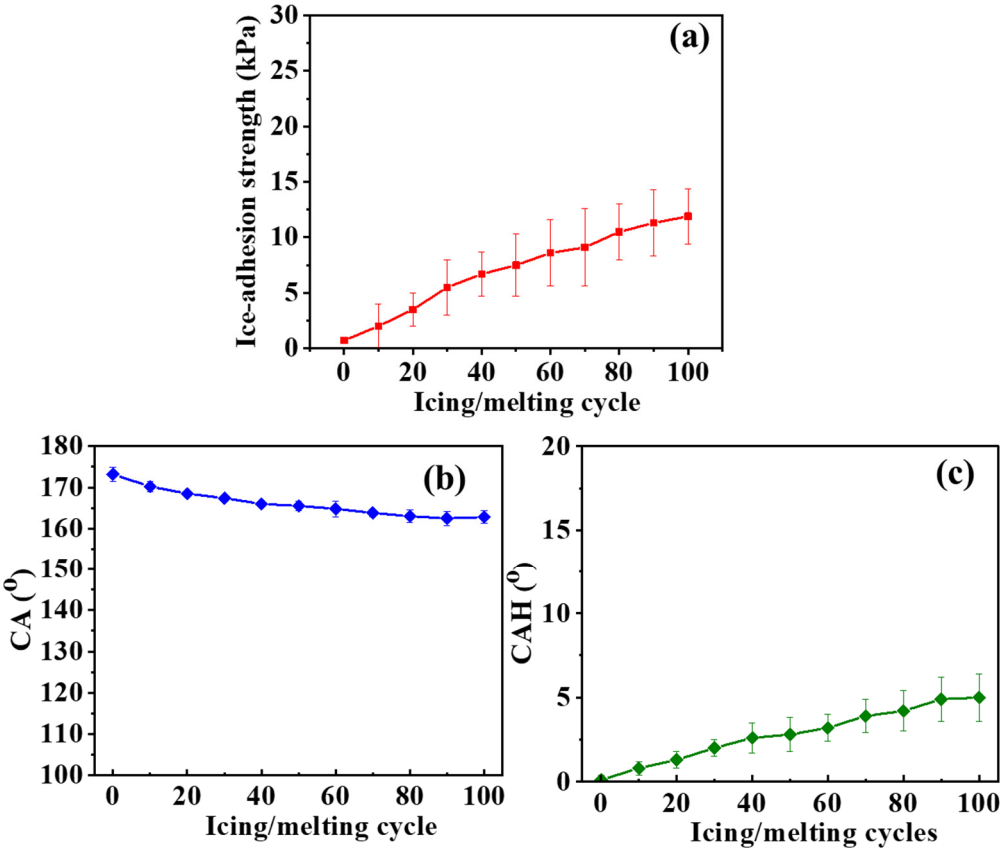

Figure 7. (**a**) Ice-adhesion strength, (**b**) CA and (**c**) CAH of the SHP surface (87.5 mA/cm^2) during icing/melting cycles.

The variation of the CA and CAH of the SHP surface with the icing/melting cycle is shown in Figure 7b,c. The initial CA of the SHP surface was 173°, and the CAH was 0.1°. As the cycle progressed, the CA gradually decreased, and CAH gradually increased. After the 100th cycle, the CA of the SHP surface decreased to 162.8°, and the CAH increased to 5.0°. It has been reported that the CA of the general SHP surface is higher than 150° while the CAH is lower than 10° [20,21].Therefore, after 100 cycles, the SHP surface still has good superhydrophobic properties, which is also an important factor for the SHP surface to maintain low ice-adhesion strength during the cycles.

The ice-adhesion strength of the SHP surface changes with the frosting/melting cycle, as shown in Figure 8a. With the increase in the number of cycles, the ice-adhesion strength of the SHP surface showed a slow upward trend. After 100 cycles, the SHP surface still maintained a low ice-adhesion strength (12.5 kPa). The variation of the CA and CAH of the SHP surface with frosting and defrosting cycles is shown in Figure 8b,c. As the cycle progressed, the CA of the SHP surface slowly decreased to 160.5°, and the CAH slowly increased to 5.3°. Although the hydrophobicity of the SHP surface decreased slightly during the frosting and defrosting process, it still had superhydrophobic properties. Therefore, the prepared SHP exhibited excellent anti-icing durability during 100 frosting/melting cycles.

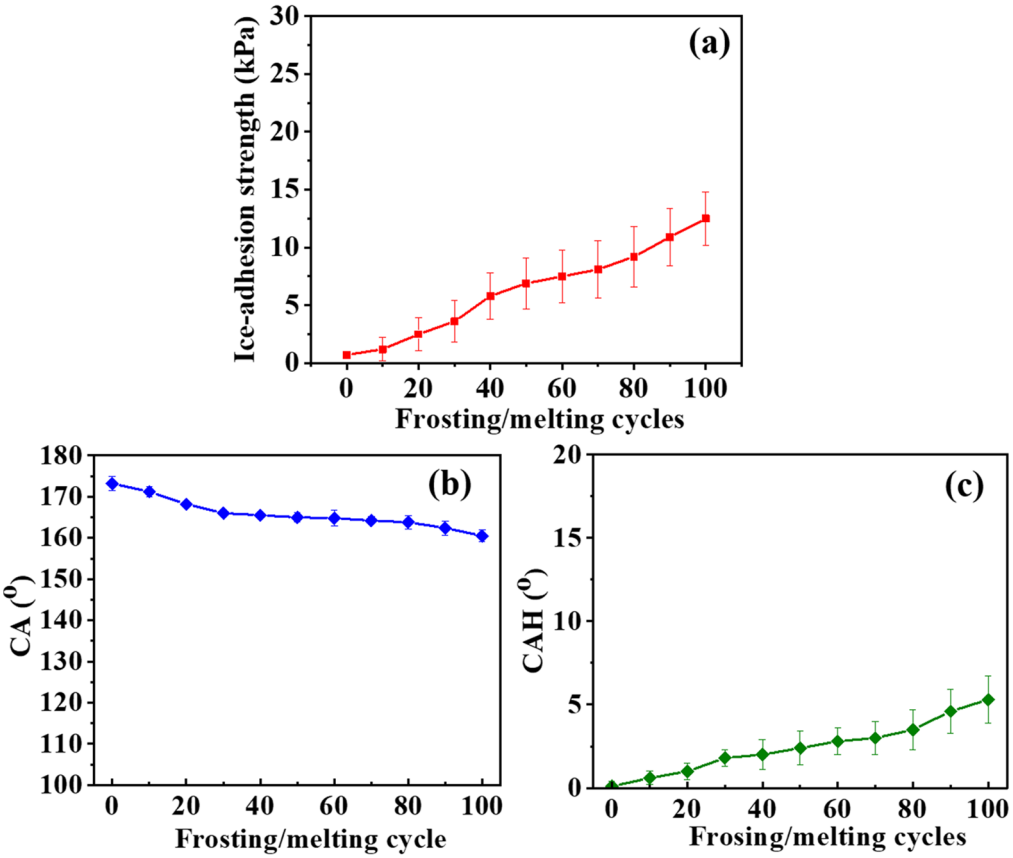

Figure 8. (**a**) Ice-adhesion strength, (**b**) CA and (**c**) CAH of the SHP surface (87.5 mA/cm^2) during frosting/melting cycles.

From the above results, 100 icing/melting and frosting/melting cycles have less damage to the anti-icing performance of the SHP surface. The reasons are as follows: first, the anodic oxidation process forms a hard porous film on the alumina substrate. The physical friction generated in the process of icing or frosting is difficult to damage the anodic oxide film. Second, the nano porous structure with a high aspect ratio stores a large number of modifiers. Although the freezing or frosting cycle can cause damage to the low surface energy material (modifier) of the SHP surface, the modifier stored in the double-layer porous structure can migrate to the damaged area under the action of capillary force, thereby restoring the anti-icing performance. To confirm the self-healing properties of the SHP surface, O_2 plasma was used to rapidly damage the low-surface-energy substances on the SHP surface. As shown in Figure 9a, the CA of the SHP surface was 173° before the damage (original). After O_2 plasma irradiation (2 min), the surface became superhydrophilic (CA = 6°), indicating that the water droplet was completely infiltrated on the damaged surface. However, after 3 h of repair, the CA recovered to 170°. The low-surface-energy molecules (FAS) on the SHP surface during the damage–repair process are illustrated in Figure 9b. The -CF_3 in FAS is damaged after plasma irradiation,

and then the FAS stored in the pores migrates outward to re-graft -CF_3 on the surface, thereby restoring superhydrophobic properties. In summary, the SHP surface with a honeycomb nanopore structure has excellent anti-icing durability.

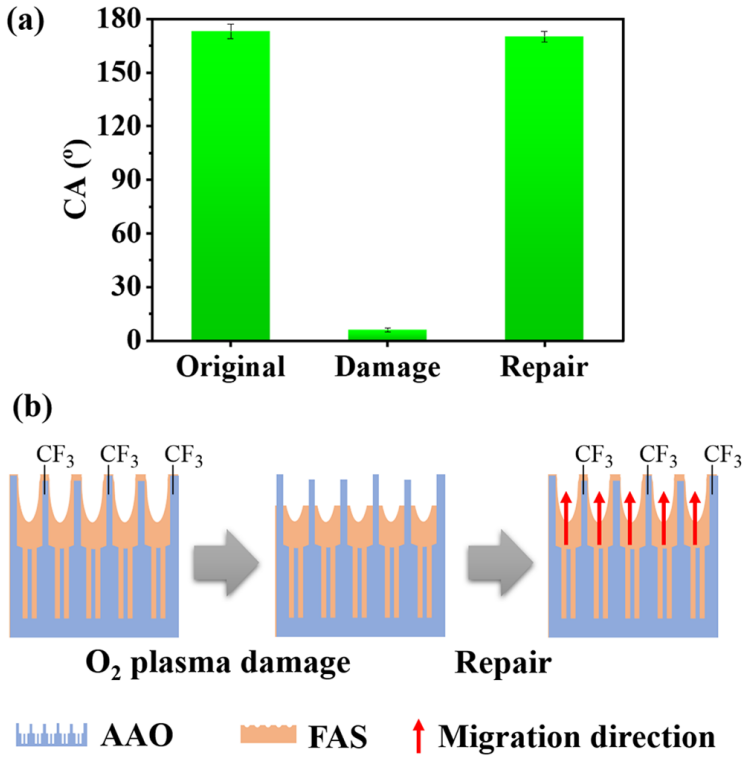

Figure 9. (**a**) CA variation of the SHP surface (87.5 mA/cm^2) and (**b**) schematic of the low-surface-energy molecules on the SHP surface during the damage–repair process.

4. Conclusions

A superhydrophobic anti-icing surface with a honeycomb nanopore structure was constructed using anodic oxidation technology combined with a vacuum infusion process. The optimal current density of the anodic oxidation was screened using wettability and anti-icing performance. The results show that the honeycomb nanopore structure with a high aspect ratio was obtained when the current density of the first step of anodic oxidation was higher than 87.5 mA/cm^2. The increase in current density not only increased the pore size and porosity, but also increased the surface roughness. When the current density was 87.5 A/cm^2, the porous surface had the best superhydrophobic performance and lowest ice-adhesion strength (0.7 kPa). The ice-adhesion strength of the SHP surface (87.5 mA/cm^2) was only 0.2% of that of the bare surface. Similarly, the SHP surface showed excellent anti-frosting performance when the current density was 87.5 mA/cm^2. The frosting rate of the SHP surface (87.5 mA/cm^2) was much slower than that of other samples, and the surface was completely covered by frost crystals after 150 min of frosting. The icing/melting and frosting/melting cycles were carried out. After 100 cycles, the SHP (87.5 mA/cm^2) still maintained a low ice-adhesion strength and excellent superhydrophobic performance, indicating that the prepared SHP surface with a honeycomb nanopore structure exhibits excellent anti-icing durability. Therefore, superhydrophobic surfaces with honeycomb nanopores have great application potential in transmission line anti-icing.

In this study, the use of FAS as a modifier played a good anti-icing effect, but the use of FAS is harmful to the environment. Therefore, a future work will be devoted to the study of non-fluorinated surface energy substances, so that the modified SHP surface has the same or better effect.

Author Contributions: Conceptualization, B.L. and Y.Y.; methodology, H.X.; software, H.X.; validation, X.D. and T.Z.; formal analysis, H.X.; investigation, B.L.; resources, X.H.; data curation, X.D.; writing—original draft preparation, B.L.; writing—review and editing, H.X.; visualization, T.Z.; supervision, Y.Y.; project administration, B.L.; funding acquisition, Y.Y. and B.L. All authors have read and agreed to the published version of the manuscript.

Funding: This research was funded by the Electric Power Research Institute of Guizhou Power Grid. Co., Ltd., China. Contract number 0666002022030101HX00001.

Institutional Review Board Statement: Not applicable.

Informed Consent Statement: Not applicable.

Data Availability Statement: The raw/processed data required to reproduce these findings cannot be shared at this time due to legal or ethical reasons.

Acknowledgments: The author would like to thank the Key Laboratory of Ice Prevention & Disaster Reducing of China Southern Power Grid Co. Ltd. (Meihuashan Base) for its help in the anti-icing test of aluminum conductors. Additionally, the authors would like to thank Jiaqi Jia from the Electron Microscope Center of Chongqing University for her help in taking micrographs of samples.

Conflicts of Interest: Bo Li has received research grants from Institute of Electric Power Science of Guizhou Power Grid Co., Ltd.

References

1. Li, L.; Luo, D.; Yao, W. Analysis of transmission line icing prediction based on CNN and data mining technology. *Soft Comput.* **2022**, *26*, 7865–7870. [CrossRef]
2. Li, J.; Wang, X.; Huang, Z.; Zhao, X.; Wang, F. Research of Preparation, Anti-icing and Anti-pollution of Super Hydrophobic Insulation Coatings. *Trans. China Electrotech. Soc.* **2017**, *32*, 61–75.
3. Li, T.; Li, J. Analysis of icing accident in South China power grids in 2008 and it's countermeasures. In Proceedings of the CIRED 2009—20th International Conference and Exhibition on Electricity Distribution—Part 1, Prague, Czech Republic, 8–11 June 2009; pp. 1–4.
4. Dalili, N.; Edrisy, A.; Carriveau, R. A review of surface engineering issues critical to wind turbine performance. *Renew. Sustain. Energy Rev.* **2009**, *13*, 428–438. [CrossRef]
5. Fan, S.H.; Jiang, X.L.; Shu, L.C.; He, P.; Liu, P.; Nie, H.Y. DC Ice-Melting Model for Elliptic Glaze Iced Conductor. *IEEE Trans. Power Deliv.* **2011**, *26*, 2697–2704. [CrossRef]
6. Peter, Z.; Farzaneh, M.; Kiss, L.I. Assessment of the current intensity for preventing ice accretion on overhead conductors. *IEEE Trans. Power Deliv.* **2007**, *22*, 565–574. [CrossRef]
7. Wang, J.; Fu, C.; Chen, Y.; Rao, H.; Xu, S.; Yu, T.; Li, L. Research and application of DC de–icing technology in china southern power grid. *IEEE Trans. Power Deliv.* **2012**, *27*, 1234–1242. [CrossRef]
8. Jiang, X.; Fan, S.; Zhang, Z.; Sun, C.; Shu, L. Simulation and experimental investigation of DC ice-melting process on an iced conductor. *IEEE Trans. Power Deliv.* **2010**, *25*, 919–929. [CrossRef]
9. Irajizad, P.; Nazifi, S.; Ghasemi, H. Icephobic surfaces: Definition and figures of merit. *Adv. Colloid Interface Sci.* **2019**, *269*, 203–218. [CrossRef] [PubMed]
10. Golovin, K.; Kobaku, S.P.R.; Lee, D.H.; DiLoreto, E.T.; Mabry, J.M.; Tuteja, A. Designing durable icephobic surfaces. *Sci. Adv.* **2016**, *2*, e1501496. [CrossRef] [PubMed]
11. Wang, L.; Zhao, H.; Zhu, D.; Yuan, L.; Zhang, H.; Fan, P.; Zhong, M. A review on ultrafast laser enabled excellent superhydrophobic anti-icing performances. *Appl. Sci.* **2023**, *13*, 5478. [CrossRef]
12. Li, W.; Zhan, Y.; Yu, S. Applications of superhydrophobic coatings in anti-icing: Theory, mechanisms, impact factors, challenges and perspectives. *Prog. Org. Coat.* **2021**, *152*, 106117. [CrossRef]
13. Li, B.; Bai, J.; He, J.; Ding, C.; Dai, X.; Ci, W.; Zhu, T.; Liao, R.; Yuan, Y. A Review on Superhydrophobic Surface with Anti-Icing Properties in Overhead Transmission Lines. *Coatings* **2023**, *13*, 301. [CrossRef]
14. Kulinich, S.A.; Farhadi, S.; Nose, K.; Du, X.W. Superhydrophobic Surfaces: Are They Really Ice-Repellent. *Langmuir* **2011**, *27*, 25–29. [CrossRef] [PubMed]
15. Farhadi, S.; Farzaneh, M.; Kulinich, S.A. Anti-icing performance of superhydrophobic surfaces. *Appl. Surf. Sci.* **2011**, *257*, 6264–6269. [CrossRef]
16. Wilson, P.W.; Lu, W.; Xu, H.; Kim, P.; Kreder, M.J.; Alvarenga, J.; Aizenberg, J. Inhibition of ice nucleation by slippery liquid-infused porous surfaces (SLIPS). *Phys. Chem. Chem. Phys.* **2013**, *15*, 581–585. [CrossRef] [PubMed]
17. Healy, W.M.; Hartley, J.G.; Abdel-Khalik, S.I. Surface wetting effects on the spreading of liquid droplets impacting a solid surface at low Weber numbers. *Int. J. Heat Mass Transf.* **2001**, *44*, 235–240. [CrossRef]
18. Golovin, K.; Dhyani, A.; Thouless, M.D.; Tuteja, A. Low-interfacial toughness materials for effective large-scale deicing. *Science* **2019**, *364*, 371–375. [CrossRef] [PubMed]

19. Kim, J.H.; Kim, M.J.; Lee, B.; Chun, J.M.; Patil, V.; Kim, Y.-S. Durable ice-lubricating surfaces based on polydimethylsiloxane embedded silicone oil infused silica aerogel. *Appl. Surf. Sci.* **2020**, *512*, 145728. [CrossRef]
20. Wong, T.-S.; Sun, T.; Feng, L.; Aizenberg, J. Interfacial materials with special wettability. *MRS Bull.* **2013**, *38*, 366–371. [CrossRef]
21. Kobina Sam, E.; Kobina Sam, D.; Lv, X.; Liu, B.; Xiao, X.; Gong, S.; Yu, W.; Chen, J.; Liu, J. Recent development in the fabrication of self-healing superhydrophobic surfaces. *Chem. Eng. J.* **2019**, *373*, 531–546. [CrossRef]